Quantifying the Ocean Coupling of Air Waves, and Why DART Data Reporting Can Be Deceptive

EMILE A. OKAL[1]

Abstract—In the context of the 2022 volcanic explosion in Tonga, we investigate the structure of the fundamental elasto-gravitational branch GR_0 of air waves, and especially their coupling to an oceanic column of variable depth. We find that the structure of the wave in the atmosphere, in particular the over-pressure component of its eigenfunction, is essentially independent of the presence and depth of an oceanic layer; normal mode theory predicts that its excitation by an explosive source in the atmosphere is also independent of water depth. The impedance of GR_0, defined as the ratio of vertical displacement of the sea surface to over-pressure at the base of the atmosphere, increases strongly with water depth and varies only marginally with frequency. It can become negative for very shallow depths and very low frequencies, but takes its classical hydrostatic value of 1 cm/mbar only for a $\sim$ 5-km deep ocean. This results in minimal maregraphic amplitudes, and hence flooding hazard, during the passage of GR_0 over very shallow seas. Finally, we find that the ratio of the sea surface displacement to the pressure signal on the seafloor, as measured for example by sensors of the DART network, increases strongly with ocean depth, but never reaches its hydrostatic value (1 cm/mbar or 10^{-4} m/Pa). In this respect, the present DART protocol in which the hydrostatic ratio is hardwired into the reporting algorithm could be considered deceptive, and should be revised.

Keywords: Atmospheric Waves, Tsunamis, DART sensors.

1. Introduction

The catastrophic eruption of the Hunga Tonga–Hunga Ha'apai [hereafter "Tonga"] volcano on 15 January 2022 featured a major atmospheric explosion which generated elasto-gravitational waves in the atmosphere with a worldwide amplitude of a few hPa (mbar) (e.g., Gusman et al., 2022), unparalleled since the 1883 explosion of Krakatau (Harkrider & Press,

1967). The principal wave circled the Earth several times, at a celerity of $\sim$ 313 m/s, practically undispersed at frequencies lower than 2 mHz, below the Brunt–Väisälä frequency characterizing the bobbing of an atmospheric particle displaced isentropically in a stable atmosphere featuring a sub-adiabatic temperature gradient (e.g., Ben-Menahem & Singh, 1981, p. 799). These properties identify the Tonga air wave as the fundamental elasto-gravitational branch GR_0 analyzed in detail by Press and Harkrider (1962), and often called a "Lamb wave", as it falls within the family of modes originally studied by Lamb (1916). However, in a previous contribution (Okal, 2024), we showed that the potential energy of the mode GR_0 was actually mostly elastic, and proposed that this surprising property was directly related to the nature of the atmosphere as a perfect gas, which mandates an intrinsic similarity between the speed of sound α and the celerity of the putative tsunami of a representative atmospheric layer under the shallow-water approximation [SWA]. In short, we concluded that a perfect gas cannot support a tsunami, defined as an oscillation between kinetic energy and gravitational potential energy in a fluid layer.

When the air wave GR_0 propagates over an ocean basin, the boundary conditions at the bottom of the atmosphere are changed, resulting in the coupling of its eigenfunction with the liquid ocean, and in particular in a deformation of the oceanic surface which can be recorded by maregraphs. Such worldwide sea level fluctuations were observed after the 1883 Krakatau event (Wharton, 1888), first interpreted as a phenomenon ancillary to an air wave by Ewing and Press (1955), and finally modeled theoretically by Harkrider and Press (1967). Because of the possibility of a maregraphic recording, this situation has

[1] Department of Earth and Planetary Sciences, Northwestern University, Evanston, IL 60208, USA. E-mail: emile@earth.northwestern.edu

occasionally been described as "a tsunami jumping a continental mass", which is of course wrong since the worldwide propagation, over both continents and oceans, is in the form of an air wave traveling at ~ 313 m/s, and as we will show, the structure of the oscillation inside an oceanic basin is fundamentally different from that of a *bona fide* tsunami.

The purpose of this paper is to investigate several aspects of the coupling between the GR_0 air wave and an oceanic column. Section 2 describes the computational strategy and the atmospheric model used. Section 3 examines the effect of an oceanic layer of variable depth on the structure of the eigenfunction in the atmosphere, which we find to be minimal. Section 4 examines the impedance Z at the ocean surface, i.e., the ratio of the vertical displacement η of the ocean surface, as measured by a maregraph, to the overpressure at the bottom of the atmosphere. Finally, Sect. 5 similarly examines the ratio D between η and the overpressure at the bottom of the ocean, which is the physical parameter measured for example by sensors of the DART network (Bernard et al., 2006). We find that both Z and D depend strongly on the depth of the oceanic column, even though both have often been assumed to take the hydrostatic value $1/(\rho_w g) \approx 1$ cm/mbar (0.1 m/kPa). These results have far-reaching consequences in terms of both the level of hazard from ocean-coupled air waves in the far field, and the scientific interpretation of DART sensor recordings.

2. Computational Strategy

In this study, we use the atmospheric model of the "Air Research and Development Command" [ARDC] (Minzner et al., 1959; Wares et al., 1960), which we truncate at an altitude of 130 km, where the particle density has already decreased by 8 orders of magnitude relative to its value at the bottom of the atmosphere (1.224 kg/m^3). The atmospheric structure is complemented by a solid Earth model inspired from PREM (Dziewonski & Anderson, 1981), extended down to a depth of 1000 km.

Figure 1a plots the particle density ρ of an oceanless model using a logarithmic scale along the ordinate axis. In order to improve the resolution of the figure, we follow Okal (2024) in using linear but variable scales in abscissæ for altitude or depth, inside the solid Earth, in the first 10 km of atmosphere, and in the upper part of the structure.

We also consider models with oceanic layers of variable depths, ranging from 100 m to 6 km. Figure 1b shows a representative model with a depth of 5 km. As a simplifying assumption, the oceans are not stratified, but rather given a constant density, $\rho_w = 1030$ kg/m^3.

Our computational strategy considers the problem of a wave propagating in a *single* "SLG" stratified medium, whose layers can be solid ("S", the solid Earth), liquid ("L", the ocean, if present) or gaseous ("G", the atmosphere). In each layer, the equations of mechanics involve both elastic and gravitational restoring forces. This is in contrast to the more traditional approach consisting of solving separately, e.g., the deformation of an elastic Earth bounded by a free surface, the tsunami of an oceanic column with a totally rigid bottom, or the air wave of an atmosphere also bounded by a rigid Earth surface, and of later attempting to work out the coupling of the resulting oscillations, hosted by physical media intrinsically incompatible with each other.

This unifying approach was originally introduced by Harkrider (1964) using a Haskell–Thomson propagator in a flat-layered system (Haskell, 1953). Then in a landmark paper, Ward (1980) showed that a tsunami represents a particular case of the Earth's spheroidal modes, whose eigenfunction penetrates (albeit weakly, of course) the solid Earth; later, the same approach was extended to the other boundary of the ocean—the atmosphere, notably by Lognonné et al. (1998), and we will use this general algorithm in the present paper. The eigenfunction is computed routinely as a 6-dimensional vector (4-dimensional in fluid layers) using Kanamori and Cipar's (1974) formalism, itself derived from earlier works (e.g., Saito, 1967).

Following these authors, boundary conditions feature an absence of deformation (zero displacements y_1 and y_3 and no change in potential y_5) at the bottom of the structure (typically taken as ~ 700 km into the solid Earth). At the top of the atmosphere (taken here at an altitude of 130 km), we impose zero overpressure and continuity of the potential
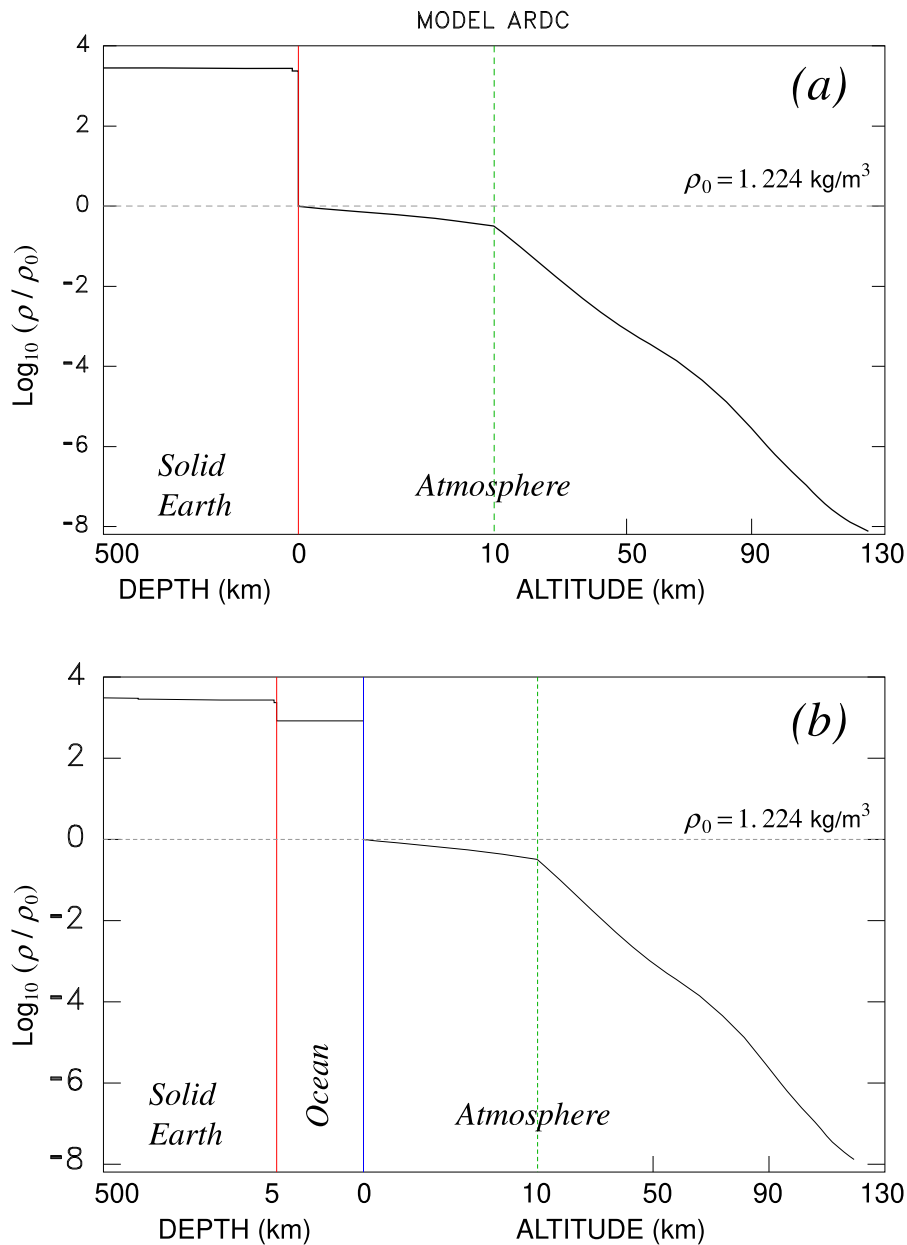
Fig. 1

Particle density ρ as a function of altitude (or depth below the atmosphere), scaled to its value at the bottom of the atmosphere (1.224 kg/m³, and plotted on a logarithmic scale. **a** Model ARDC without an ocean. The horizontal scale is linear, but varies within the solid Earth (left of the red vertical line), in the first 10 km of the atmosphere (left of the green dashed line), and in the upper atmosphere. Note the fast decay of ρ_{air}, which loses 8 orders of magnitude at the top of the model. **b** Model ARDC with a 5-km deep ocean, left of the blue vertical line. The conventions are similar to **a**, with the same horizontal scale in the ocean and in the first 10 km of atmosphere

component y_5 with its value predicted in the absence of mass from Laplace's equation for the relevant value of the orbital degree l (Saito, 1967).

We emphasize that this algorithm includes the elastic and gravitational components of the restoring force in any medium; in particular when applied to the case of a classic tsunami wave in an oceanic

column, it automatically takes into account the effects of the finite elasticity of water, and of gravity inside the solid substratum, as recently studied, e.g., by Watada et al. (2014). A fundamental advantage of the normal mode formalism is that it resolves seamlessly the question of the effect of the fine structure of the interface between the major layers of the SLG system, *e.g.,* sedimentary layers between the ocean and the rigid crust (Lognonné et al., 1998; Okal, 1988; Ward, 1980).

Additionally, the normal mode approach lends itself to the effortless computation of the excitation of any type of wave by a point source, derived directly from the classic paper by Gilbert (1971), with essentially no change in coding with respect to classical synthetic seismograms. In all instances, the theory remains linear and in many cases it was used successfully to recover quantitative estimates of the source (i.e., seismic moments) remarkably consistent with independently published values (*e.g.,* Okal and Talandier, 1991; Okal, 2007).

Finally, we have verified that results from the normal mode approach are consistent with those using Harkrider's (1964) formalism.

3. The Structure of GR_0: Largely Insensitive to the Oceanic Column

In Fig. 2, we examine the eigenfunction of the GR_0 wave computed around $T = 1000$ s using the normal mode formalism with orbital degree $l = 127$. Figure 2a shows the vertical displacement, y_1 in the notation of Saito (1967), normalized to its value at the bottom of the atmosphere, and plotted using a logarithmic scale. Note that it grows very fast in the first few km, stabilizes around 3 orders of magnitude about 10 km height, and then gains another 4 orders of magnitude at the top of the structure. Such very large displacements just express the much reduced particle density ρ_{air}: very little mass is actually moved around at those heights. The irregularities in the plot around 20–35 km are an artifact of y_1 changing sign and featuring two nodes, the logarithmic plotting scale mandating the use of its absolute value. Figure 2b similarly plots the component y_2, which in a fluid is the opposite of the overpressure p.

It features a much more regular decay with height from its value at the bottom of the atmosphere, by about 6 orders of magnitude to the top of the structure. In this respect, it constitutes a better descriptor of the general eigenfunction than y_1. Finally, inside the solid Earth, both components decay regularly with depth; in this case, y_2 becomes the normal stress component σ_{rr}.

In Fig. 3, we target two periods (600 s, *Left*; and 2000 s, *Right*), and examine the influence of an oceanic layer on y_2, the opposite of the overpressure, scaled to a common value of 1 at the bottom of the atmosphere; it is taken as representative of the structure of the eigenfunction. The variable y_2 is plotted linearly along the horizontal scale. The vertical scale represents depth below the atmosphere (positive values) or altitude into it (negative values). The scale is linear between an altitude of 15 km and a depth of 10 km. Logarithmic scales are used outside this window. Various colors are used to represent the profile of y_2 for various ocean depths h, from 0 (no ocean, black) to 6 km (red). The most remarkable property is that, at both periods, the profile of y_2 in the atmosphere is totally independent of h; in practice, the various curves plot on top of each other. In the presence of an oceanic column, the overpressure keeps increasing with depth inside the water, but the coupling remains small and does not affect the structure of the wave in its main domain, namely the atmosphere. As shown on Fig. 4, this property is confirmed by the fact that the phase and group velocities also remain remarkably constant as a function of h, as does the energy integral, $[I_1 + l(l + 1) I_2]$ in the notation of Saito (1967), computed for a common normalization of $y_2 = 1$ at the base of the atmosphere.

In short, the atmospheric wave remains essentially insensitive to the presence or absence of an underlying medium of finite elasticity; its propagation and its structure are entirely controlled by the atmosphere, i.e., by the medium which supports it in the first place. Its prolongation into the solid Earth and/or a potential oceanic layer keeps an ancillary character which does not affect the fundamental structure of the eigenfunction inside the atmospheric column. A parallel can be drawn with the case of a classical oceanic tsunami, whose propagation is unaffected by
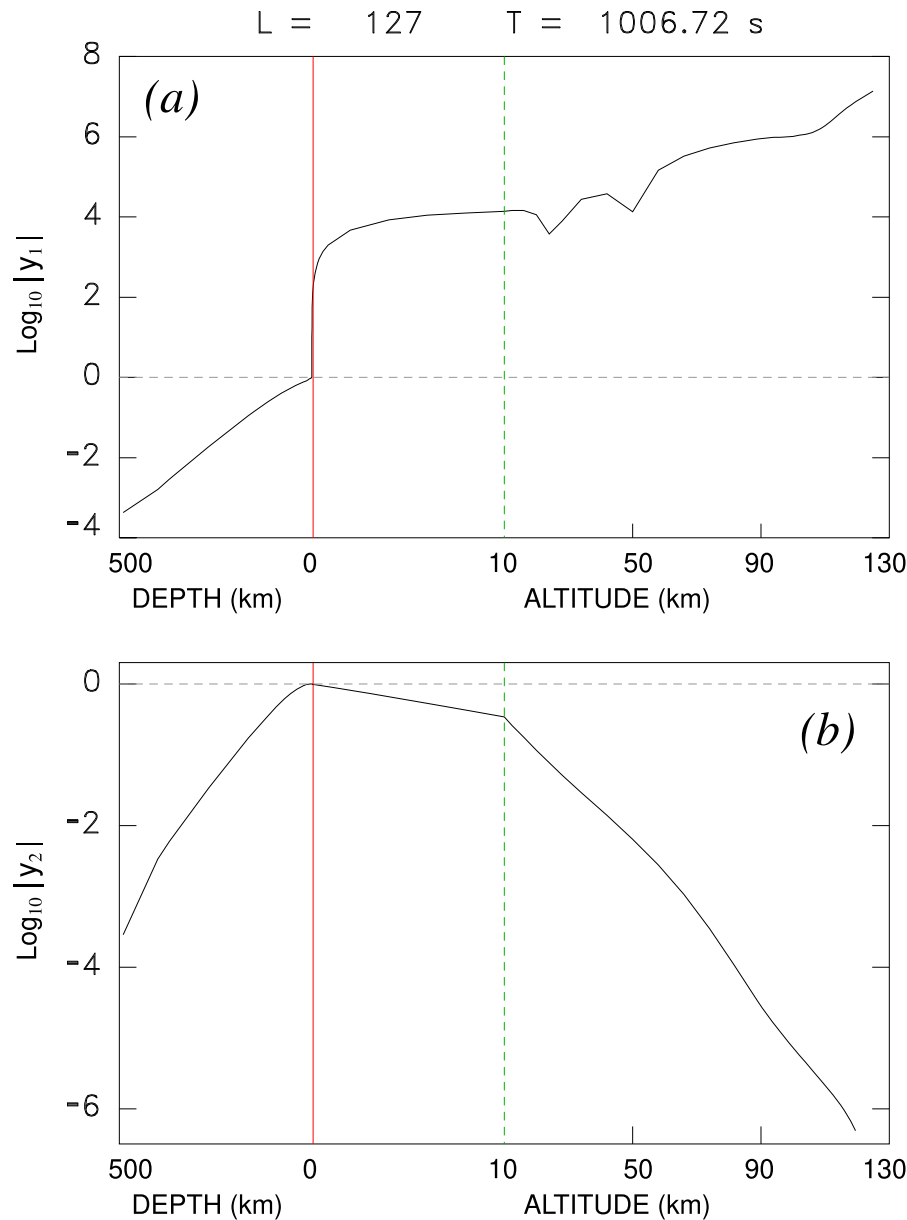
Fig. 2

a Vertical displacement component y_1 of the eigenfunction of the branch GR_0 around $T = 1000$ s ($l = 127$) for the ocean-less structure. The horizontal scaling is similar to that of Fig. 1a. y_1 is normalized to its value at the bottom of the atmosphere, and plotted using a logarithmic scale. **b** Same as **a** for the [opposite of the] overpressure, y_2, similarly normalized to its value at the bottom of the atmosphere

the presence of the atmosphere, even though its eigenfunction is indeed prolonged upwards, all the way to the ionosphere where it can result in significant perturbations as detected during major tsunamis (Artru et al., 2005; Occhipinti et al., 2006); or to the case of a standard seismic Rayleigh wave, which is continued into the oceanic column where it can be detected (Freitag & Okal, 2020; Simon et al., 2021), but without significant effect on its dispersion properties.

We now consider the excitation of the air wave by a dynamic source located in the atmosphere. In the normal mode framework, and for a fluid layer, the only possible such source is an explosion, which can
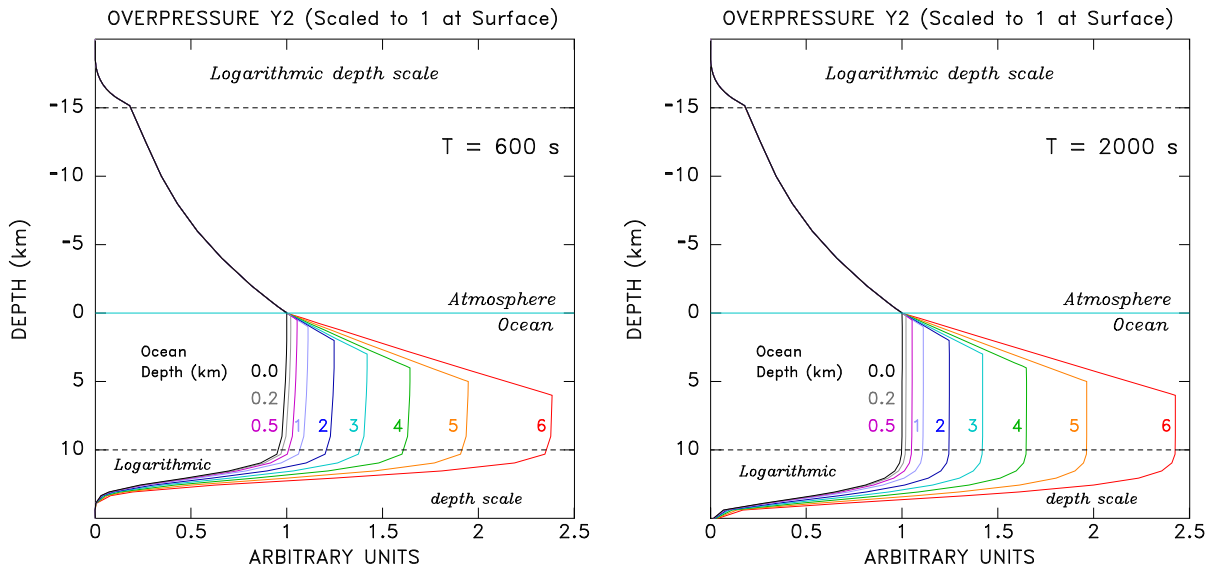
Fig. 3
Overpressure $-y_2$ (scaled to 1 at the bottom of the atmosphere) as a function of depth in the ocean (positive values) or altitude in the atmosphere (negative values) for a variety of ocean depths, color-coded from 0 (no oceans, black) to 6 km (red). The vertical scale is linear between a depth of 10 km and an altitude of 15 km, and logarithmic otherwise. Note that all curves plot on top of each other in the atmosphere, and differ only in the oceanic and solid layers. **a** Period $T = 600$ s; **b** Period $T = 1000$ s

be conceptually characterized by an isotropic moment M_0, through an excitation coefficient N_0:

$$N_0 = -\frac{2l+1}{4\pi\,\omega^2\,[I_1 + l(l+1)I_2]} \cdot \frac{y_2\,(r_s)}{K_s} \quad (1)$$

obtained by setting $\mu_s = 0$ in Eq. (2) of Okal (1978). In (1), r_s is the radius from the center of the Earth to the source, and K_s the bulk modulus at the source. As we have seen, both y_2 in the atmosphere and the energy integral $[I_1 + l(l+1)\,I_2]$ are independent of water depth, so we anticipate that N_0 should also be. This is verified on Fig. 5, where we target the same three periods as in Fig. 4 (600, 1000 and 2000 s), and plot the absolute value of N_0 in the first 20 km of the atmosphere (normalized to a common value of 1 for y_2 at the bottom of the atmosphere), for all nine oceanic models previously considered. We plot each curve with the same color code as in Fig. 3, from no ocean (black) to $h = 6$ km (red). However, it is immediately apparent that all curves plot essentially on top of each other, which expresses that *the excitation of GR_0 by an explosion in the lower atmosphere is independent of the presence of an oceanic layer, or of its thickness.*

It is possible to draw a parallel between these properties and those of very long-period seismic Rayleigh waves, whose eigenfunctions are essentially unaffected by the presence of an oceanic column, as long as the depth h of the water layer remains much smaller than the wavelength Λ. Note here that, while the dispersion of mantle Rayleigh waves has long been known to be sensitive to the presence and depth of an oceanic layer (e.g., Kausel et al., 1974), this effect is due to variations in the structure of the crust and upper mantle (e.g., Yu & Mitchell, 1979), but not to the mere presence of the water layer. Indeed, we have verified that at $T = 180$ s ($l = 50$; $\Lambda \approx 800$ km), the phase velocity of a Rayleigh wave varies by only 0.2% when the ocean depth is increased from 1 to 5 km, while keeping a constant solid Earth structure. Similarly, the various excitation coefficients at a representative depth of 40 km vary by at most 1.5%. In both instances (mantle Rayleigh waves and GR_0 air waves), this is an illustration of the Rayleigh-Ritz variational principle, namely that the eigenfunction is stationary with respect to a small variation of structure.
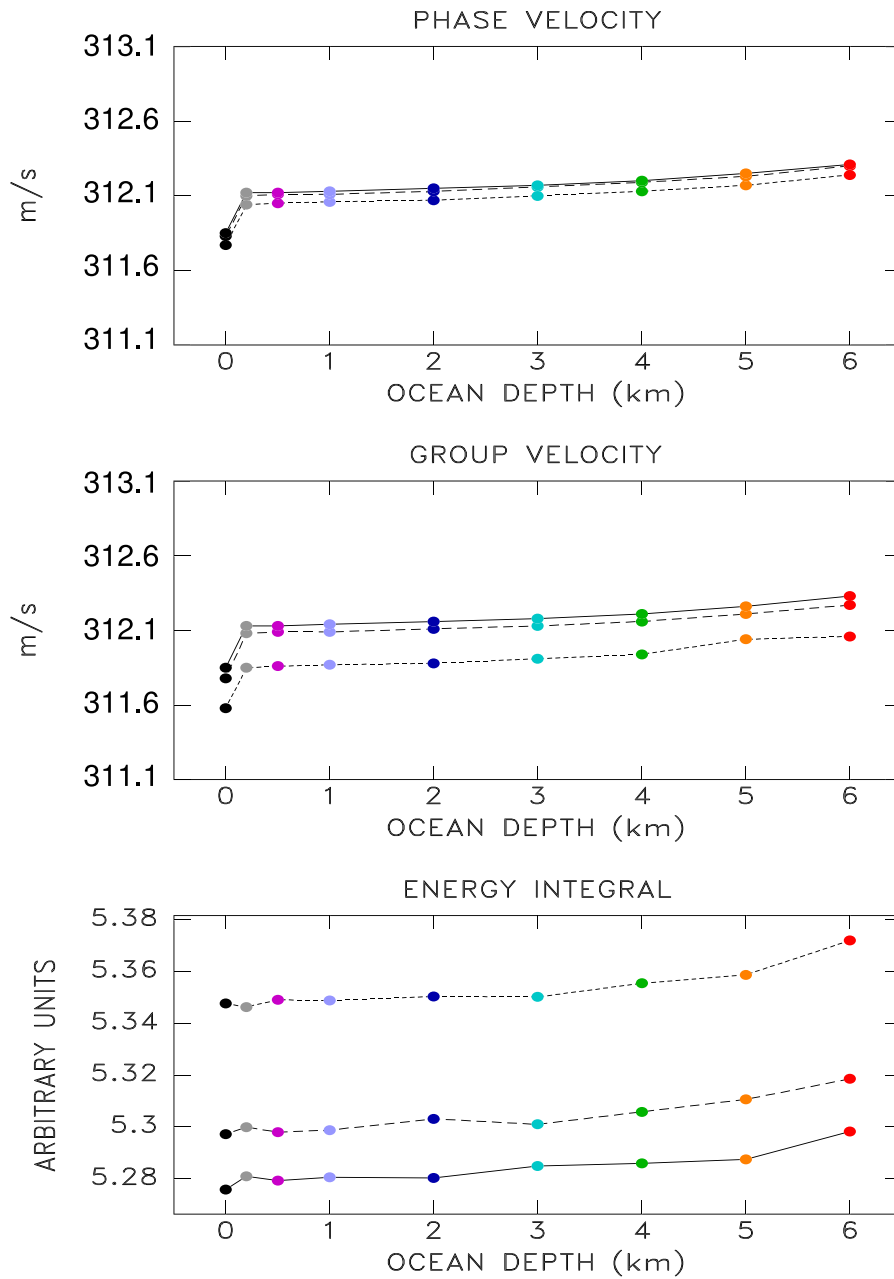
Fig. 4

Variation of phase velocity C *(Top)*, group velocity U *(Center)* and energy integral $[I_1 + l(l+1)I_2]$ *(Bottom)* as a function of the depth h of the oceanic column, for three target periods (600 s, dotted line; 1000 s, dashed line; 2000 s, solid line). Individual values are color-coded as in Fig. 2. Note the remarkable constancy of the velocities with both period and h. While the energy integral expectedly varies with period, it remains largely independent of h
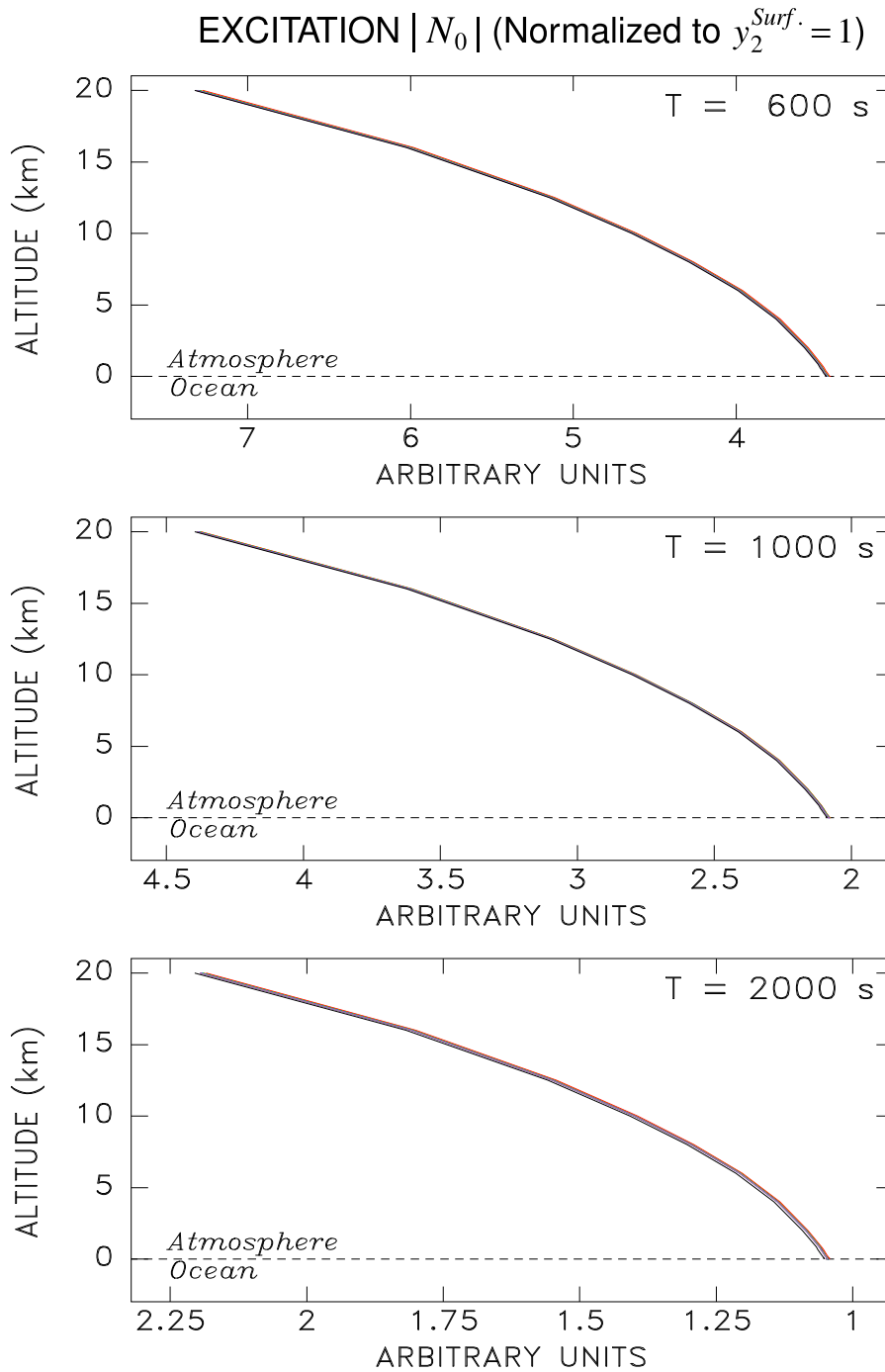
EXCITATION $|N_0|$ (Normalized to $y_2^{Surf.} = 1$)

Fig. 5

Excitation of the air wave branch GR_0 by an explosive source as a function of the altitude of the source, at 3 representatives periods. Plotted is the absolute value $|N_0|$ defined by (1), scaled to a common value $y_2 = 1$ at the bottom of the atmosphere, using a common linear horizontal scale for all ocean depths at each of the three periods. Each ocean depth is color-coded as in Fig. 3; however, all curves plot on top of each other, indicating the independence of N_0 on depth

4. Response of the Ocean to the Air Wave GR_0

In this section, we focus on the dynamic response of an oceanic column to the passage of an air wave, namely on the value of the vertical motion η of the surface of the ocean resulting from the overpressure component p of the GR_0 air wave. We characterize it through the impedance ratio at the base of the atmosphere,

$$Z \;=\; \frac{\eta}{p} \;=\; -\frac{\eta}{y_2} \qquad (2)$$

where y_2 is the normal stress component of the eigenfunction in the normal mode formalism. Since we have shown that y_2 is largely insensitive to the presence (or depth) of an ocean, this ratio will allow the interpretation of a maregraphic record of the wave (such as those obtained in the very far field following the 1883 Krakatau explosion) in terms of the properties of the air wave in its home medium, the atmosphere. Harkrider and Press (1967) examined variations in Z as a function of frequency, but fixed the ocean thickness at $h = 5$ km. They found that at low frequencies, Z approaches its hydrostatic value ($1/\rho_w g \approx 10^{-4}$ m/Pa = 1 cm/mbar), but could increase greatly when the celerity of GR_0 is reduced to values close to $\sqrt{gh}$, characteristic of the propagation of a genuine tsunami. In addition, except in special cases described in Sect. 5 below, Z is *positive*, which is in contrast to the case of a storm surge.

By contrast, we consider here variations in Z both with period and ocean depth. Figure 6 is a color-coded contour of Z in the frequency range 0.1–2 mHz ($T = 500$–10,000 s) and for depths h varying from 0.1 to 6 km. Clearly, Z increases strongly and regularly with water depth h, but decreases only marginally with increasing period T, at least in the frequency domain selected, i.e., when the celerity of GR_0 remains larger than that of a regular tsunami. For the typical ocean depth (5 km) used by Harkrider and Press (1967), that condition would occur only when the group velocity U drops considerably due to coupling of the branch with acoustic "S" modes (Press & Harkrider, 1962), in the vicinity of the Brunt–Väisälä frequency. In much shallower waters, this would require even slower GR_0 celerities, which coupling with acoustic modes cannot provide. The agreement

reported by Harkrider and Press (1967) between Z in the limit $\omega \to 0$ and the hydrostatic value (1 cm/mbar) is a pure artifact of their choice of $h = 5$ km, which incidentally overestimates the average depth of the world's oceans, $\overline{h} \approx 3.7$ km.

An intriguing result of Fig. 6 is the existence of a small domain where Z takes a negative value (black shading), namely for very shallow depths ($h \leq 200$ m) and very long periods (in practice greater than 1600 s). In this regime, an underpressure ($y_2 > 0$) will result in a positive surge η. In the absence of an oceanic layer, an overpressure at the bottom of the atmosphere will always result in a subsidence of the substratum, but in its presence and for sufficiently large h and ω, the layer acts to reverse the impedance and create a positive bulge at the ocean surface. On the other hand, if the layer is too thin, it cannot provide this effect, and Z remains negative. This is obviously scaled to the wavelength Λ, hence the dependence on frequency. Indeed, the boundary of the black domain on Fig. 6 ($Z = 0$) can be reasonably approximated by the line $kh \approx 10^{-3}$, where $k = 2\pi/\Lambda = \omega/C$, with $C = 313$ m/s, shown as the small purple dots on Fig. 6. A tentative explanation of this property is given in Sect. 6.

It is interesting to note that a similar situation ($Z < 0$) is observed at the eye of a hurricane, where severe underpressure results in flooding of coastlines upon landfall (notwithstanding the additional dynamic surge created by the winds). At a given coastal location, a hurricane is a relatively long-lived phenomenon, lasting several hours to a day, and thus may correspond to the limit $\omega \to 0$ of an atmospheric system. In that particular case, a perfect hydrostatic equilibrium is achieved, with the impedance Z taking the value $-1/(\rho_w g)$.

Note finally that the broad variations of Z with period T and primarily with ocean depth h rule out the concept of a simple hydrostatic response of the sea level η to the overpressure p carried by the air wave.

The general patterns of Z are illustrated spectacularly on Fig. 7, which presents maregrams and barograms recorded across the Bering Sea following the Tonga explosion. The Bering Sea is divided structurally into a deep Southwestern basin, and an extremely shallow Northeastern half ($h < 50$ m for the most part). Figure 7a shows maregrams at the three
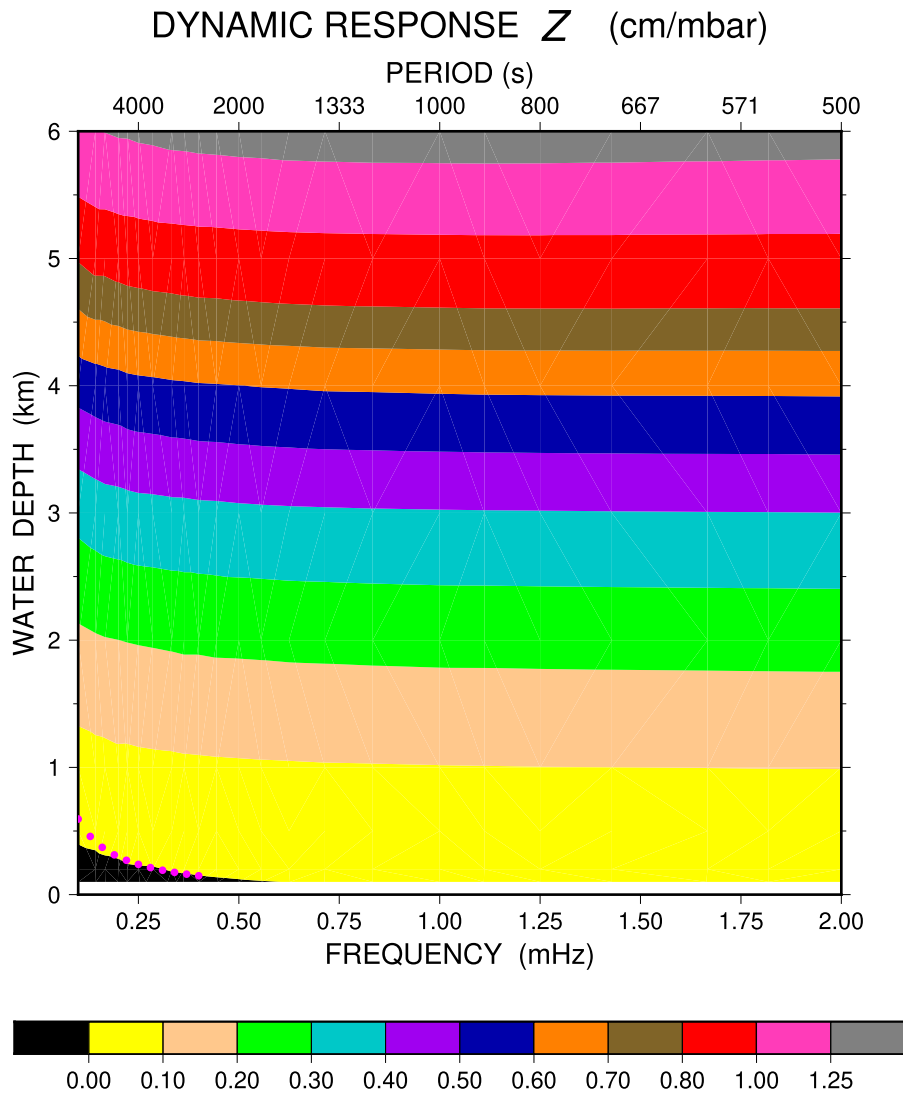
DYNAMIC RESPONSE Z (cm/mbar)

Fig. 6

Color-coded contour of the dynamic response ratio Z (Eq. 3) as a function of frequency and ocean depth. Note a strong dependence on h, but a minor one on ω. At very long periods and very shallow depths, there is a small region of negative response; the small purple dots plot the line $kh = 10^{-3}$. See text for discussion

locations Adak, St. Paul (Pribilof Islands), and Nome (Alaskan mainland). Adak is a relatively small island (711 km^2) surrounded by deep water. The arrival of the long-period GR_0 wave at Adak is poorly recorded (solid arrow), but later components result in significant oscillations reaching 40 cm zero-to-peak. By contrast, no sea surface oscillations are recorded at Nome, where the continental shelf extends for several hundreds of km at depths less than 50 m. Finally, St. Paul in the Pribilof Islands sits at the edge of the continental platform and features an intermediate behavior. We have verified, using available nearby meteorological stations, that the overpressure of the air wave remains essentially constant over the entire area (Fig. 7b).

The origin of such sea-surface oscillations whose amplitude correlate remarkably with the depth of the water column, can be sought in the analysis of the air wave undertones, which Mizutani and Yomogida (2023) have identified as significant contributors, as
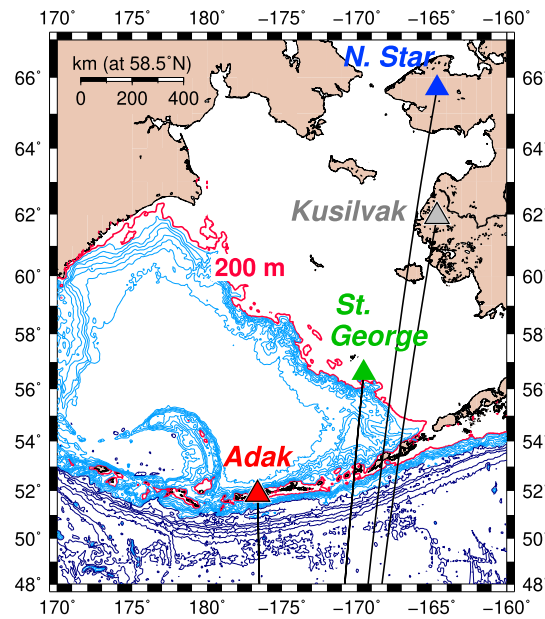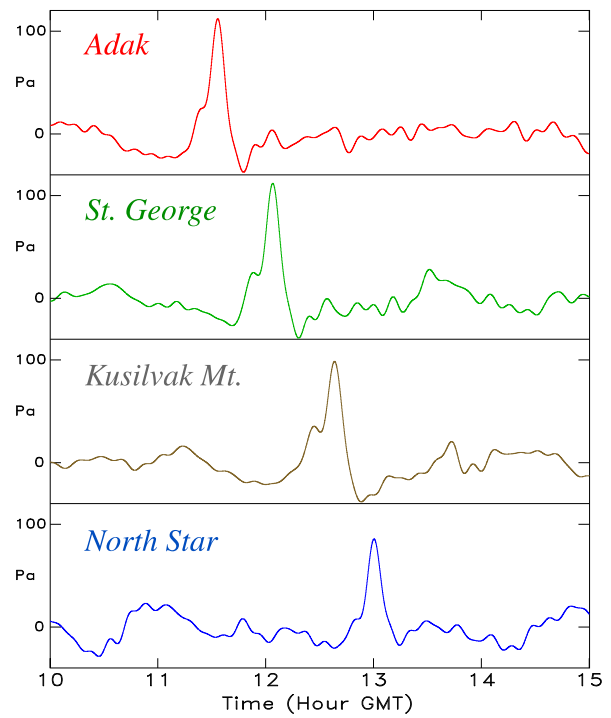
a   BERING SEA -- 15 JAN 2022
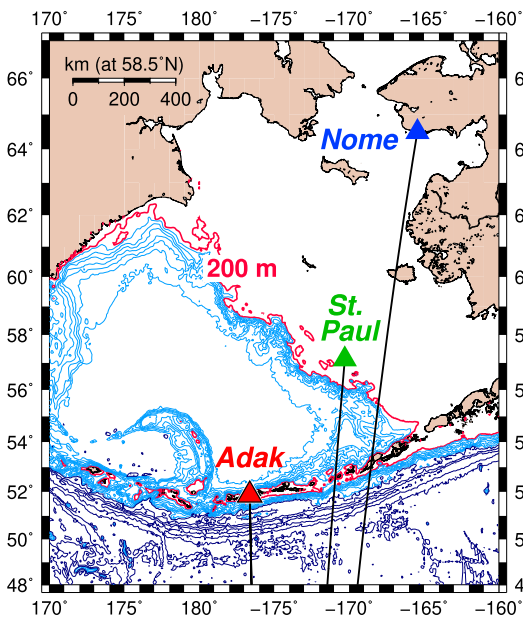
TIDAL GAUGE RECORDS

HOURS (GMT; 15 JAN 2022)
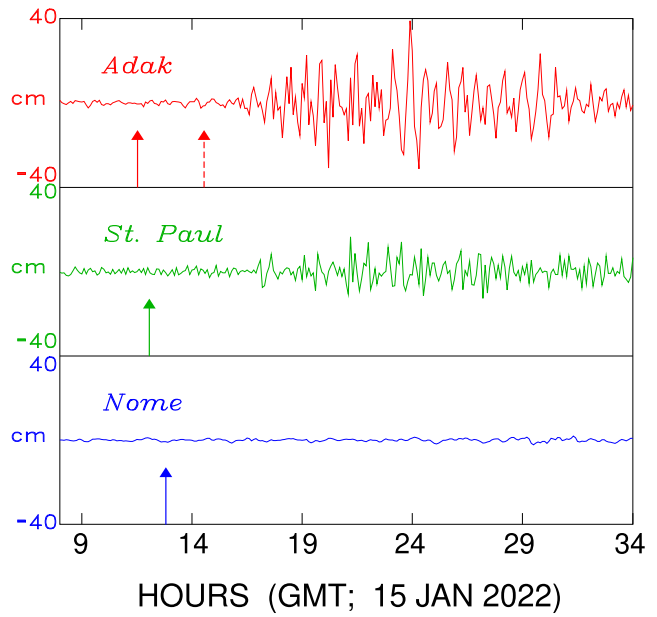
b   BERING SEA -- 15 JAN 2022

BAROMETRIC RECORDS

a *Left:* Map of the Bering Sea with the three maregraphic stations Adak, St. Paul and Nome. Bathymetric contours are at intervals of 500 m down to 3500 m (light blue), and 1000 m deeper (dark blue); additionally, the 200-m isobath is shown in pink to highlight the shallow Northern basin. *Right:* Time series of maregrams at the three stations following the 2022 Tonga explosion, plotted on the same scale. **b** Same as **a** for barometric time series at four meteorological stations available in the vicinity of the maregraphic stations. This time, note the similarity in amplitudes, pointing out different dynamic responses Z

originally suggested by Harkrider and Press (1967) in the case of GR_2. The name "Pekeris waves" has recently been proposed for such harmonics of the branch GR_0 (Watanabe et al., 2022). Indeed, for the particular branch GR_2, we have verified a generally similar behavior, i.e., a strong decrease of the surface impedance Z with decreasing water depth. For these modes, and in the low-frequency limit ($f < 1$ mHz), Z is found to be as high as 15 cm/mbar for $h = 6$ km,
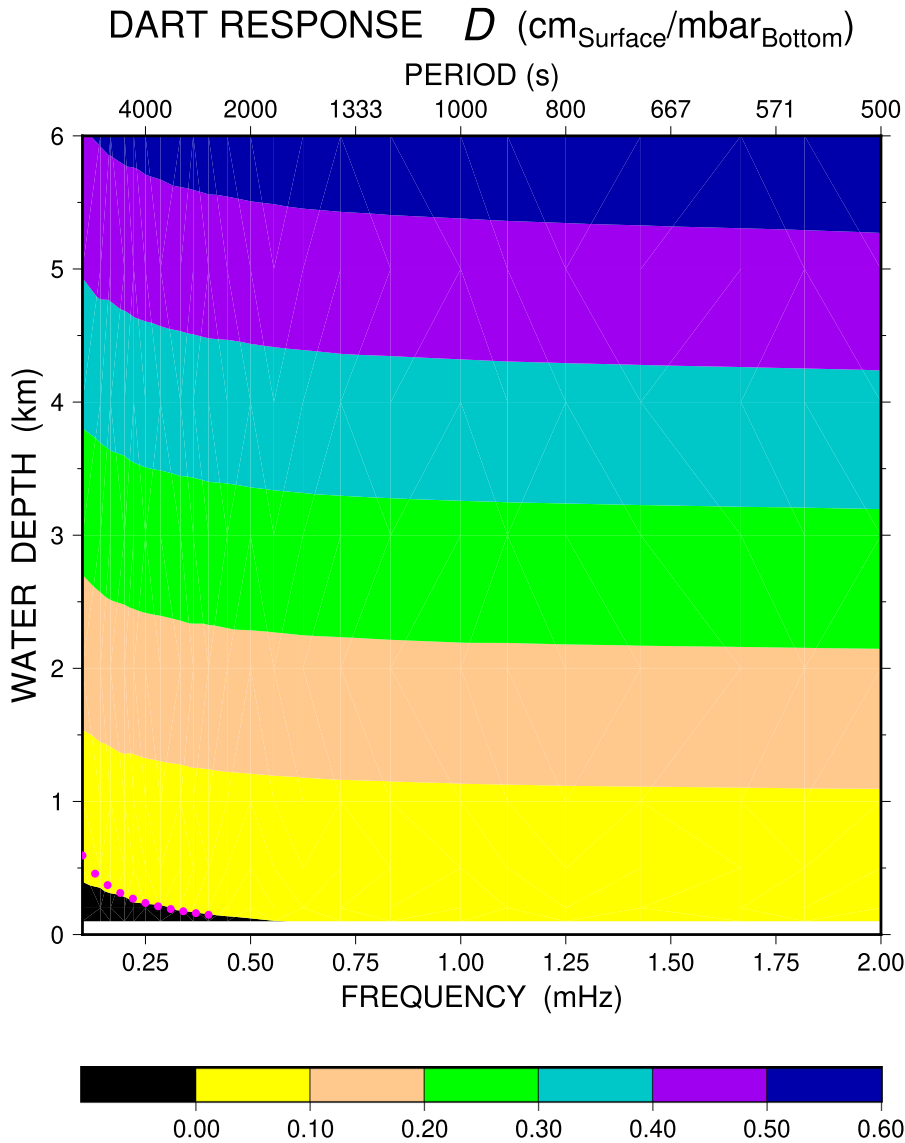

Fig. 8
Color-coded contour of the ratio D of vertical amplitude at the sea surface to overpressure at the sea bottom, in cm/mbar, as a function of ocean depth and frequency. The palette is common to Fig. 6, as are the small purple dots, which delineate the same region of negative D

but falls to 0.1 cm/mbar for $h = 1$ km. The impedance Z also exhibits a stronger increase with frequency than for the fundamental GR_0, reaching values of up to 100 cm/mbar for $f = 2$ mHz and $h = 5$ km. The origin of such high values of Z lies in the coupling of the Pekeris modes with the genuine tsunami branch ("GW" in those authors' notation), which is possible only in deep water ($h \approx 5$ km; Adak). Note in particular that for a tsunami under the SWA in an atmosphere-free ocean, Z would be infinite; in practice in the presence of a realistic atmosphere, $1/Z$ takes a small *negative* value on the order of -25 Pa/m.

5. The Pressure at the Bottom of the Ocean and the Response of a DART Sensor

In this section, we examine the response of a seafloor DART sensor to the passage of a GR_0 air wave. We are motivated by the results of Fig. 3, which clearly document the effect of ocean depth on the overpressure at the seafloor. Figure 8 is similar in concept to Fig. 6, but this time contours the ratio

$$D \; = \; \frac{\eta}{p^{Bott.}} \qquad (3)$$

of the vertical sea surface displacement η to the overpressure $p^{Bott.}$ on the sea floor. D^{-1} can be regarded as the response of a DART sensor to a disturbance of the ocean's surface. The color palettes used in Figs. 6 and 8 are identical.

The general behavior of D is similar to that of Z on Fig. 6, namely it increases weakly with frequency, but strongly with water depth. However, in the range of parameters considered, D has a maximum value of 0.58 cm/mbar and *never* reaches the "hydrostatic" ratio of 1 cm/mbar. In very shallow waters and at very long periods, D features the same region of negative values as Z on Fig. 6.

These results would appear to contradict the classic paradigm that all long "tsunami" waves in shallow water feature a ratio D equal to the hydrostatic value of ~ 1 cm/mbar. However, as discussed above, the prolongation of the air wave into the oceanic column does not constitute a tsunami wave, of which it features neither the propagation

characteristics, nor the structure of its eigenfunction; as a result, the apparent contradiction is moot. This point will be discussed in more detail in Sect. 6 below, in the context of the operation of DART sensors. In a more general context, it serves to emphasize that not all oscillations of an oceanic layer can be regarded as tsunamis, let alone ones obeying the SWA, a condition necessary to feature the "hydrostatic" ratio $D = 1/(\rho_w g) \approx 1$ cm/mbar.

A further interpretation is given on Fig. 9, where we contour $R = Z/D$ which represents the dimensionless ratio of overpressures at the bottom and top of the ocean, in other words the gain of the water column acting as an amplifier of the pressure at the bottom of the atmosphere. This ratio is always positive and greater than 1, as hinted from the profiles in Fig. 3. It goes to 1 when $h \rightarrow 0$, which simply expresses that a very thin film of water cannot provide any amplification of the pressure signal. R also decreases very weakly with increasing frequency, a behavior opposite that of Z and D.

In view of its weak dependence on frequency, we regroup on Fig. 10 the dataset of values of D and plot them for 24 sampled frequencies, as a function of h only, for depths $h \geq 200$ m. As expected, we note that all curves plot very close to each other. The full dataset can be regressed linearly as

$$D \; = \; 0.093 \, h \; - \; 0.014 \qquad (4)$$

where h is in km and D in cm/mbar, as shown by the red dashed line on Fig. 10. Regression slopes at individual frequencies increase weakly with frequency, from 0.088 (cm/mbar)/km (8.8 GPa^{-1}) at 0.1 mHz to 0.097 (cm/mbar)/km (9.7 GPa^{-1}) at 2 mHz.

6. Discussion and Conclusion

In order to discuss some physical aspects of the coupling of a GR_0 air wave with an oceanic column, we regroup in Table 1 critical parameters obtained for a representative selection of combinations of depths h and periods T. We consider a deep ocean ($h = 5$ km) and a shallow one ($h = 1$ km), and three periods spanning the frequency range of Figs. 6, 8 and 9. In addition, we explore the case of a very thin film of
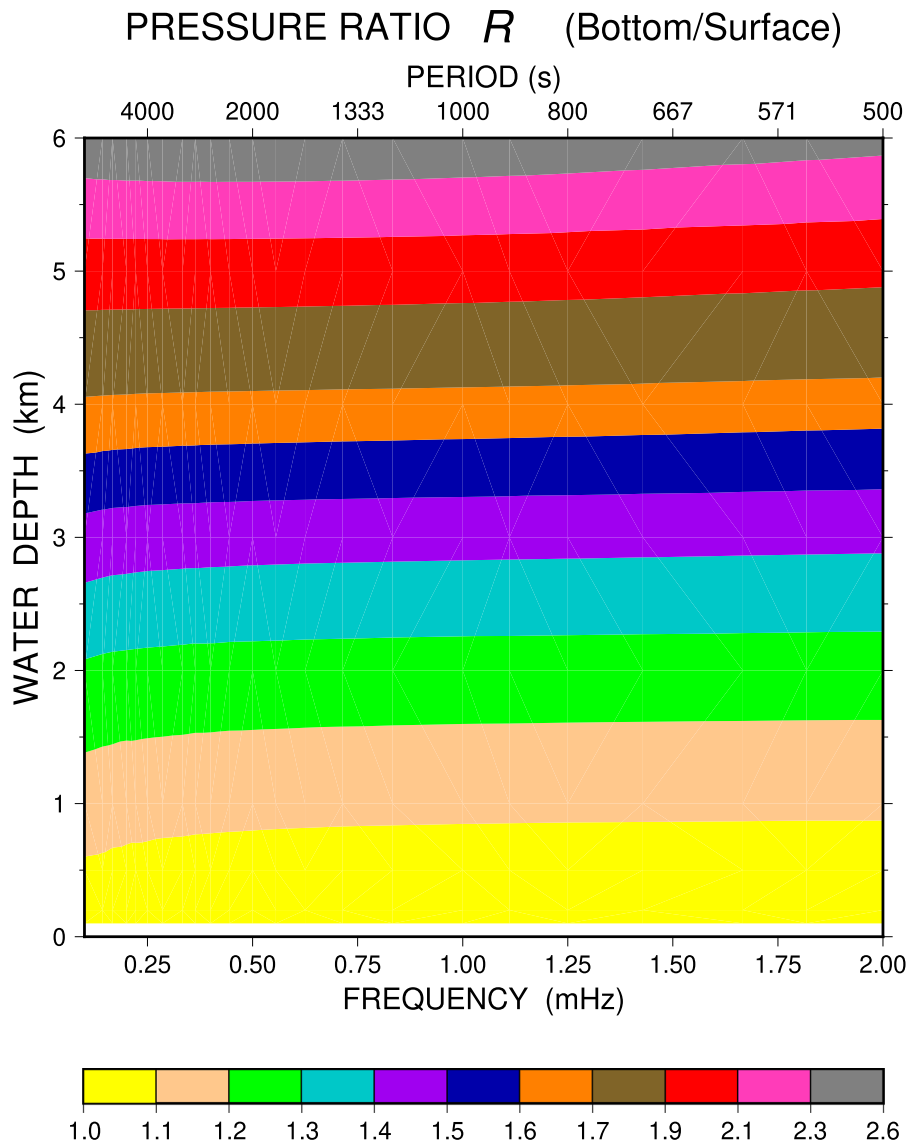
PRESSURE RATIO R (Bottom/Surface)

Fig. 9

Color-coded contour of the ratio R of overpressure at the bottom and surface of the oceanic layer, as a function of ocean depth and frequency. Note that R is always positive, greater than 1, increases with depth and only marginally with frequency

water ($h = 100$ m) at very low frequency (0.1 mHz) which leads to negative values of Z and D.

A legitimate question concerns the possible influence of the finite elasticity of the substratum (both liquid and solid) on the structure of the eigenfunction and in particular its dispersion. We are motivated in this respect by the work of Watada et al. (2014) who showed that this explained minor delays in observed group arrival times of tsunami waves

with respect to those computed by standard algorithms, as observed more than 60 years ago (Nakamura & Watanabe, 1961) and widely confirmed following the major tsunamis of the early 2000s (Hébert et al., 2009; Rabinovich et al., 2011). For this purpose, we also consider a model in which we artificially increase by a factor of 10 the seismic velocities in the solid Earth and oceanic layers, while leaving unchanged the atmospheric ones and the
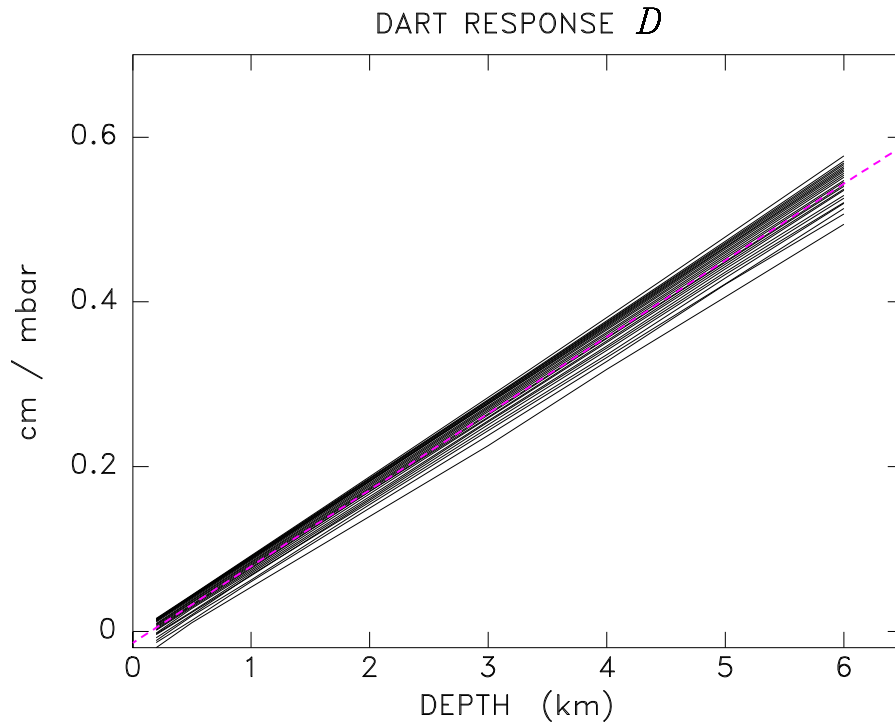
DART RESPONSE D

Fig. 10
Same dataset as in Fig. 8, plotted as a function of depth only between 200 m and 6 km, for each of 24 frequencies sampled in this study. Note that all traces plot next to each other, highlighting the primary dependence of D on h. The red dashed line is the regression (2)

densities ρ in all layers. This has the effect of multiplying by 100 the elastic moduli of the substratum, and we will refer to it as "the stiffer model", for which the relevant parameters are listed in *italics* in all boxes of Table 1. A further experiment will consist of changing the water density ρ_w while keeping all other parameters fixed.

The first two entries of Table 1 (period T and phase velocity C) confirm that the water depth h has practically no effect on the dispersion of the air wave, nor does the rigidity of the substratum. This illustrates, once again, that even though it is weakly coupled to the ocean and the solid Earth, the structure of the air wave is totally controlled by the atmosphere.

We then list the three parameters defined above (Z, D and $R = Z/D$), which are extracted from the dataset in Figs. 6, 8 and 9, as discussed above. Note that in the stiffer model, Z decreases less at very low frequencies, but otherwise the three parameters remain comparable in the two models. This illustrates

that they are not controlled by the elastic properties of the substratum, but rather almost completely by the depth of the oceanic column.

We similarly list the ratio of the vertical displacements at the top and bottom of the water layer, as well as the ratio of the vertical displacement to overpressure at the bottom of the ocean. In the case of an oceanic tsunami, and under the assumption that it is prolonged into the solid Earth in the form of the "pseudo-Rayleigh" wave of a homogeneous half-space, we had shown (Okal, 2003; Eq. 1) that this ratio is expected to be

$$\Psi = \frac{y_1^{Bott.}}{p^{Bott.}} = -\frac{3}{4}\frac{1}{\mu k} = -\frac{1}{Z'} \quad (5)$$

where μ is the rigidity of the solid, k the wavenumber and Z' is Z in Okal's (2003) notation; this ratio characterizes the *impedance* of the solid. Equation (5) is valid in the limit when the phase velocity of the wave is much smaller than the shear velocity of the solid, and therefore, the concept extends to the air

Table 1

Selected parameters for representative models of GR_0 air waves

	$h = 5$ km			$h = 1$ km			$h = 100$ m
l	12	127	256	12	127	256	12
T (s)	10271.29 *10270.51*	1006.2 *1006.2*	500.3 *500.3*	10274.60 *10274.40*	1006.6 *1006.6*	50.5 *500.5*	10275.0 *10274.9*
C (m/s)	311.8 *311.8*	312.0 *312.0*	311.9 *311.9*	311.7 *311.7*	311.3 *311.5*	311.8 *311.8*	311.7 *311.7*
Z (cm/mbar)	0.773 *0.937*	0.903 *0.972*	0.901 *0.957*	0.0609 *0.1055*	0.0965 *0.1083*	0.1001 *0.1085*	−0.025 *0.0093*
D (cm/mbar)	0.409 *0.476*	0.460 *0.488*	0.467 *0.491*	0.0551 *0.0951*	0.0869 *0.0973*	0.0901 *0.0977*	−0.024 *0.0092*
R	1.892 *1.967*	1.966 *1.993*	1.930 *1.949*	1.105 *1.109*	1.111 *1.112*	1.111 *1.111*	1.010 *1.010*
$\eta / y_1^{Bott.}$	−12.48 *−1446.8*	−81.46 *−8652.0*	−155.94 *−16443.9*	−1.664 *−285.49*	−14.90 *−1671.7*	−28.35 *−3079.9*	0.734 *−39.75*
$y_1^{Bott.} / p^{Bott.}$ (cm/mbar)	−32.7 *−0.329*	−5.64 *-0.056*	−2.99 *−0.030*	−33.1 *−0.333*	−5.84 *−0.058*	−3.17 *−0.0317*	−33.2 *−0.333*
$\mu^{Eff.}$ (GPa or 10^{10}dyn/cm^2)	121.7 *12099*	66.7 *6676*	62.3 *6248*	120.20 *11946*	64.6 *646.5*	58.7 *5887*	119.9 *11955*
PREM Upper mantle μ (GPa or 10^{10}dyn/cm^2)		67.3 *6734*			67.3 *6734*		67.3 *6734*
FACTOR ρ_w *halved*	26.1 *27.8* *54.2*	30.0 *30.8* *60.2*	30.5 *31.2* *61.1*	21.2 *22.1* *43.7*	24.0 *24.1* *48.2*	24.2 *24.4* *48.5*	20.4 *21.1* *41.9*
$-\phi$ (Eq.9; GPa^{-1}) ρ_w *halved*	8.38 *8.81* *17.23*	9.50 *9.71* *19.07*	9.73 *9.92* *19.48*	8.49 *8.82* *17.47*	9.56 *9.66* *19.22*	9.67 *9.74* *19.38*	8.52 *8.82* *17.54*

In each box, the first line (roman type) features a regular solid Earth model (inspired from PREM), while for the second one (in italics), seismic velocities in the substratum (ocean and solid Earth) have been artificially multiplied by 10. Note that the units selected for μ allow the direct multiplication of parameters in common, practical units (densities in g/cm^3 and seismic velocities in km/s)

wave in the SLG system, where the ratio is typically of order 1/10. Note finally the minus sign in (5), since we consider the overpressure p rather than the radial shear stress y_2 used in Okal (2003). In our notation, Ψ is always negative, which is expected since thermodynamics mandate that a positive overpressure on a solid Earth half-space should always result in a subsidence ($y_1^{Bott.} < 0$).

Conversely, for any computed air wave, we can define an "effective rigidity" of the solid Earth as

$$\mu^{Eff.} \; = \; -\frac{3}{4}\frac{1}{\Psi}\cdot\frac{1}{k} \; = \; -\frac{3}{4}\cdot\frac{a}{l\,\Psi} \qquad (6)$$

where a is the radius of the Earth, and l the relevant orbital degree. $\mu^{Eff.}$ is listed at the bottom of Table 1 where it is compared with the actual value of the rigidity in the sub-Moho, upper mantle layers of the Earth model used (67 GPa for $\rho = 3.37\,\text{g/cm}^3$ and $\beta = 4.47$ km/s, and 100 times more in the stiffer model). The agreement is excellent for $h = 5$ km and a period of 1000 s, where the tail of the wave can be expected to sample the solid over 1/4 of a wavelength, or ~ 80 km. At shorter periods, it feels the influence of the less rigid crustal layers, and $\mu^{Eff.}$ decreases, while at much longer periods, $\mu^{Eff.}$ is essentially doubled, reflecting the increased densities and seismic velocities of the lower mantle.

Based on these results, we then proceed to explore the physical response of an SLG structure, and in particular the origin of the occasionally negative values of Z and D. In Sect. 3, we showed that the overpressure $p = -y_2$ is a robust descriptor of the eigenfunction in the atmosphere, largely oblivious to whatever substratum may be underlying it. Thus, we consider a wave with overpressure $p^{Surf.}$ at the bottom of the atmosphere, which we take as positive for illustrative purposes. An oceanic layer then functions as an **amplifier** of p from top to bottom, with a gain R which can be regressed from Fig. 9 as

$$R \; = \; 0.219\,h \; - \; 0.0175\,f \; + \; 0.929 \qquad (7a)$$

where h is in km and f in mHz. In view of the small dependence of R on f, and of its obvious value of 1 for $h = 0$, the simpler regression

$$R \; = \; 1 + \kappa h \text{ with } \kappa = 0.198 \; \approx \; 0.2\,\text{km}^{-1} \quad (7b)$$

appears more meaningful. We do not have at this point a simple physical explanation for this property of a water column.

The resulting overpressure at the bottom of the ocean then yields a vertical displacement $y_1^{Bott.}$ of the latter given by (5), where the parameter Ψ is totally independent of the presence and thickness of the water layer, and is controlled only by the combination of the rigidity of the solid Earth and the wavenumber (Okal, 2003), the former depending slightly on the latter on account of the structural stratification of realistic models of the solid Earth. At this stage, $y_1^{Bott.} / p^{Bott.} = \Psi$ is always *negative* from simple thermodynamic arguments, and so is $y_1^{Bott.} / p^{Surf.} = \Psi\,(1 + \kappa h)$.

As we move up the water column, y_1 will evolve through its partial derivative $(\partial y_1 / \partial z)$ which according to Hooke's law is related to the ambiant overpressure through

$$\frac{\partial y_1}{\partial z} + l\,\frac{\partial y_3}{\partial x} \; = \; \frac{\partial y_1}{\partial z} + k\,l\,y_3 \; = \; \frac{p}{K} \qquad (8)$$

where $l\,y_3$ is the horizontal particle displacement, k is the wavenumber, and K the bulk modulus of the water.

A systematic investigation of the structure of the eigenfunction reveals that the horizontal displacement, $l\,y_3$, is essentially constant throughout the water column (varying less than 5% from top to bottom); note that this property is identical in the case of tsunami waves under the SWA, but the ellipticity at the surface is significantly different. In addition, we find that the second term in the left hand side of (8), $l\,(\partial y_3 / \partial x)$, always remains much larger, by a factor of 20–30 ("*FACTOR*" in Table 1), than the right hand side (p/K), which amounts to saying that the water behaves like an incompressible fluid. Moreover, for a given ocean and solid Earth model, this term remains independent of h and l. When scaled to $p^{Bott.}$, it takes the value

$$\phi \; = \; l\,\frac{\partial y_3 / \partial x}{p^{Bott.}} \; \approx \; \frac{-1}{\rho_w\,C^2} \qquad (9)$$

in practice about $-10\,\text{GPa}^{-1}$, C being the phase velocity of the wave. We have no simple physical explanation for this property, but have verified the dependence of (9) on ρ_w by artificially halving the density of the ocean while keeping all other parameters unchanged (see Table 1).

Consequently, the gradient of vertical displacement in the water column will be

$$\frac{\partial y_1}{\partial z} \; \approx \; -l\,\frac{\partial y_3}{\partial x} \; = \; -\phi\,p^{Bott.} \qquad (10)$$

always positive and constant throughout the water

column. One thus predicts that the displacement at height z from the ocean floor will be

$$y_1(z) = y_1^{Bott.} - z\phi\, p^{Bott.} = p^{Bott.}(\Psi - z\phi) \quad (11)$$

With Ψ and ϕ both negative, (11) predicts a node of y_1 at a height

$$z_0 = \frac{\Psi}{\phi} = \frac{3}{4}\frac{\rho_w C^2}{\mu}\cdot\frac{1}{k} \quad (12)$$

inversely proportional to the wavenumber k, but independent of h. Conversely, the surface displacement η and hence the ratio Z will become negative if this height is greater than the thickness h of the water column, or for a given thickness h, if $k < k_0$ with

$$k_0\, h = \frac{h\, l_0}{a} = \frac{3}{4}\frac{\rho_w C^2}{\mu} \approx 10^{-3} \quad (13)$$

The values predicted by (13) for depths $h = 100, 200,$ and 500 m are $l_0 = 64, 32$ and 12, respectively, using $\mu = 67$ GPa. In practice, a systematic computation along the GR_0 branch shows transition to negative η at $l = 77, 35$ and 6 respectively. In the first two cases, the agreement is good; in the last one, it deteriorates, on account of the increase in effective rigidity due to deeper penetration of the eigenfunction at the very large wavelengths involved. Finally, in the—unrealistic—stiffer model, and as documented in Table 1, the gradient ϕ is essentially unchanged, but since $y_1^{Bott.}$ is much smaller in absolute value, y_1 becomes positive at a greater depth, and for all combinations of h and T, the amplitude η on the surface is positive for a positive overpressure p.

This discussion provides an explanation for the existence of a domain of negative values of Z and D, and for its delineation along the line (13), as noted above in Figs. 6 and 8.

Finally, it is interesting to contrast this situation with the case of a genuine oceanic tsunami under the SWA, where the bottom overpressure will be $p^{Bott.} = \rho_w g\, \eta$, and the value of Ψ unchanged from (5), resulting in

$$y_1^{Bott.} = -\frac{3}{4}\frac{\rho_w g}{\mu k}\cdot\eta \quad (14)$$

while the horizontal displacement of the water column will be $l\, y_3 = \eta\, /\, kh$, independent of z, and

$$\frac{\partial y_1}{\partial z} = -\phi^{Tsu} \approx -l\frac{\partial y_3}{\partial x} = \frac{\eta}{h} \quad (15)$$

As a result, the height z_0 of the node of y_1 will be written as

$$\frac{z_0}{h} = \frac{3}{4}\frac{\rho_w g}{\mu k} = -\frac{y_1^{Bott.}}{\eta} \quad (16)$$

In other words, in a tsunami, the node will scale with h in the exact same [absolute] ratio that the vertical displacement at the bottom scales with that at the surface, always an exceedingly small number; indeed $z_0 > h$ would require $l < (3/4)(\rho_w ga\, /\, \mu) \approx 0.72$ for $\mu = 67$ GPa, which is clearly impossible. This remark stresses once again the fundamental difference in structure between a genuine tsunami and the prolongation of an air wave into the oceanic column.

The results of Sect. 4 have significant and somewhat sobering consequences regarding far-field hazard potentially due to ocean-coupled air waves. In the first place, coastlines are found to be effectively protected by the presence of wide continental platforms with shallow bathymetry. The example of the Northern Bering Sea is reproduced at such locations as the Adriatic Sea and the Bay of Biscay. Note that the decrease of dynamic response over shallow waters is in contrast to the amplification of a genuine tsunami under Green's Law (Green, 1837), although extensive propagation of a tsunami over very shallow waters eventually leads to breaking of the wave. Second, as detailed by Harkrider and Press (1967) and observed, e.g., at Adak (Fig. 7a) in deep water, the maximum surface amplitude occurs at a group time following propagation at the regular tsunami velocity, as would be predicted using routine warning algorithms. Warnings issued for the earlier arrival of the air wave could actually convey a false sense of safety given the smaller dynamic response at such group times. Finally, the amplitudes recorded in the far field from the Tonga ocean-coupled air waves, generated by overpressures on the order of 1 to a few hPa (mbar), have remained decimetric (zero-to-peak); run-up values of 1 m or greater are generally attributable to the genuine tsunami generated independently of the air wave. Such amplitudes are probably equivalent to their counterparts during the 1883 Krakatau explosion, as inferred by Harkrider

and Press (1967), based on data compiled by Wharton (1888). While the maximum size of any future similar explosion remains speculative, it can be simply stated that the exceptional events of 1883 and 2022 failed to generate in the far field truly catastrophic sea waves comparable to those of tsunamis due to mega-earthquakes at subduction zones.

Regarding the results of Sect. 5, the properties of the ratio D have very serious consequences on the present reporting of data from DART sensors, which in its current form could be regarded as deceptive.

We recall that the DART instruments (and those of comparable systems) consist of pressure sensors collecting data on the ocean floor. Their concept originated in the 1960s (Vitousek & Miller, 1970). Following the unexpected detection of the 1979 Petatlán, Mexico tsunami by Filloux (1982), a number of prototypes were developed (Bernard and Milburn, 1985; González et al., 1991) and the project became operational in the early 2000s. It presently constitutes a fundamental component of real-time tsunami warning infrastructure (Bernard et al., 2006).

However, a major problem with the present data reporting protocol of the DART network is that the sensors measure the pressure signal $p^{Bott.}$ but *report it* as an equivalent surface displacement η (in units of meters) using the hydrostatic conversion factor $(1 / \rho_w g \approx 1$ cm/mbar$)$. That ratio is adequate in the case of tsunami waves under the SWA, which is of course the main purpose of the DART project. However, even for tsunami waves, but outside the SWA, it already becomes inappropriate and must be replaced with

$$\frac{\eta}{p^{Bott.}} \;=\; \frac{\cosh kh}{\rho_w \, g} \qquad (17)$$

where k is the wavenumber of the tsunami (*e.g.,* Dean & Dalrymple, 2000). Equation (17) is illustrated by the fact that DART sensors do not respond to sea swell; it also explains the classical observation that a submarine does not feel weather-related sea swell.

The situation is only exacerbated when considering waves of a different structure for which the use of the hydrostatic ratio has simply no physical justification. For example, Freitag and Okal (2020) have discussed the response of a seafloor pressure sensor to

a long-period seismic Rayleigh wave and shown that it functions as an accelerometer with a gain proportional to water depth, and as a velocity sensor when recording a P wave. In the case of a GR_0 wave, Sect. 5 has shown that the response parameter D will never take the hydrostatic value 1 cm/mbar, but rather will always be smaller. Equation (4) can serve as an empirical substitute for the hydrostatic ratio in a wide range of frequencies and ocean depths.

In this respect, the uninformed user of DART time series reported in meters, trusting this information at face value, will always **overestimate** the surface displacement which actually took place during the measurement. We have further verified on a preliminary dataset that a similar bias will also take place for the Pekeris undertone GR_2, mentioned by Harkrider and Press (1967) as a potentially significant contributor to the maregraphic record, although its D values will generally be larger than those of the fundamental GR_0, indeed reaching 1 cm/mbar for $h = 6$ km and $f = 2$ mHz. This would lead to a systematic error in the interpretation of the relative amplitude of the two wavetrains.

> In order to prevent any further misinterpretation of the data from DART and comparable networks, we call on the operators of such systems to report the data in its actual form as measured on the ocean floor, namely as a *pressure* time series expressed in units of hPa, rather than as an equivalent ocean height.

Declarations

REFERENCES

Artru, J., Dučić, V., Kanamori, H., Lognonné, P., & Murakami, M. (2005). Ionospheric detection of gravity waves induced by tsunamis. *Geophysical Journal International, 160*, 840–848.

Ben-Menahem, A., & Singh, S. J. (1981). *Seismic waves and sources*, (1108 pp.). New York: Springer-Verlag.

Bernard, E. N., & Milburn, H. B. (1985). Long-wave observations near the Galápagos Islands. *Journal of Geophysical Research, 90*, 3361–3366.

Bernard, E. N., Mofjeld, H. G., Titov, V. V., Synolakis, C. E., & González, F. I. (2006). Tsunami: Scientific frontiers, mitigation, forecasting, and policy implications. *Philosophical Transactions of the Royal Society of London, Series A, 364*, 1989–2007.

Dean, R. G., & Dalrymple, R. A. (2000). *Water wave mechanics for engineers and scientists*. World Scientific.

Dziewonski, A.M., & Anderson, D.L. (1981). Preliminary reference Earth model. *Physics of the Earth and Planetary Interiors*, 25, 297−356.

Ewing, W. M., & Press, F. (1955). Tide-gage disturbances from the great eruption of Krakatoa. *Transactions of the American Geophysical Union, 36*, 53–60.

Filloux, J. H. (1982). Tsunami recorded on the open ocean floor. *Geophysical Research Letters, 9*, 25–28.

Freitag, L., & Okal, E. A. (2020). Preliminary results from a prototype ocean-bottom pressure sensor deployed in the Mentawai Channel, Central Sumatra, Indonesia. *Pure and Applied Geophysics, 177*, 5119–5131.

Gilbert, J. F. (1971). Excitation of the normal modes of the Earth by earthquake sources. *Geophysical Journal of the Royal astronomical Society, 22*, 223–226.

González, F. I., Mader, C. L., Eblé, M. C., & Bernard, E. N. (1991). The 1987–88 Aleutian Bight tsunamis: Deep-ocean data and model comparisons. *Natural Hazards, 4*, 119–139.

Green, G. (1837). On the motion of waves in a canal of variable depth. *Cambridge Philosophical Transactions, 6*, 457–462.

Gusman, A. R., Roger, R., Noble, C., Wang, X., & Power, W. (2022). The 2022 Hunga Tonga-Hunga Ha'apai Volcano air-wave generated tsunami. *Pure and Applied Geophysics, 179*, 3511–3525.

Harkrider, D. G. (1964). Theoretical and observed acoustic-gravity waves from explosive sources in the atmosphere. *Journal of Geophysical Research, 69*, 2595–5321.

Harkrider, D. G., & Press, F. (1967). The Krakatoa air-sea waves: an example of pulse propagation in coupled systems. *Geophysical Journal of the Royal astronomical Society, 13*, 149–159.

Haskell, N. A. (1953). The dispersion of surface waves in multilayered media. *Bulletin of the Seismological Society of America, 43*, 17–24.

Hébert, H., Reymond, D., Krien, Y., Vergoz, J., Schindelé, F., Roger, J., & Loevenbruck, A. (2009). The 15 August 2007 Peru earthquake and tsunami: Influence of the source characteristics on the tsunami heights. *Pure and Applied Geophysics, 166*, 211–232.

Kanamori, H., & Cipar, J. J. (1974). Focal process of the great Chilean earthquake, May 22, 1960. *Physics of the Earth and Planetary Interiors, 9*, 128–136.

Kausel, E., Leeds, A. R., & Knopoff, L. (1974). Variations of Rayleigh wave phase velocities across the Pacific Ocean. *Science, 186*, 139–141.

Lamb, H. (1916). *Hydrodynamics* (4th ed., p. 708). Cambridge University Press.

Lognonné, P., Clévédé, E., & Kanamori, H. (1998). Computation of seismograms and atmospheric oscillations by normal-mode summation for a spherical Earth model with realistic atmosphere. *Geophysical Journal International, 135*, 388–406.

Minzner, R. A., Champion, K. S. W., & Pond, H. L. (1959). *The ARDC model atmosphere*. Air Force Office of Scientific Research.

Mizutani, A., & Yomogida, K. (2023). Source estimation of the tsunami later phases associated with the 2022 Hunga Tonga volcanic eruption. *Geophysical Journal International, 234*, 1885–1902.

Nakamura, K., & Watanabe, H. (1961). Tsunami forerunner observed in case of the 1960 Chile tsunami of 1960. In *Report of the Chilean tsunami of May 24, 1960 as observed along the coast of Japan*. Committee for field investigation of the Chilean tsunami of 1960.

Occhipinti, G., Lognonné, P., Alam-Kherani, E., & Hébert, H. (2006). Three-dimensional waveform modeling of ionospheric signature induced by the 2004 Sumatra tsunami. *Geophysical Research Letters, 33*(20), L20104.

Okal, E. A. (1978). A physical classification of the Earth's spheroidal modes. *Journal of Physics of the Earth, 26*, 75–103.

Okal, E.A. (1988). Seismic parameters controlling far-field tsunami amplitudes: A review. *Natural Hazards, 1*, 67−96.

Okal, E.A. (2003). Normal modes energetics for far-field tsunamis generated by dislocations and landslides. *Pure and Applied Geophysics, 160*, 2189−2221.

Okal, E.A. (2007). Seismic records of the 2004 Sumatra and other tsunamis: A quantitative study. *Pure and Applied Geophysics, 164*, 325−353.

Okal, E. A. (2024). On the nature of potential energy in atmospheric gravity waves, or why the atmosphere cannot sustain a tsunami, *Pure and Applied Geophysics, 181*, 1–25.

Okal, E.A., & Talandier, J. (1991). Single-station estimates of the seismic moment of the 1960 Chilean and 1964 Alaskan earthquakes, using the mantle magnitude M_m. *Pure and Applied Geophysics, 136*, 103–126.

Press, F., & Harkrider, D. G. (1962). Propagation of acoustic-gravity waves in the atmosphere. *Journal of Geophysical Research, 67*, 3889–3908.

Rabinovich, A. B., Woodworth, P. I., & Titov, V. V. (2011). Deep-sea observations and modeling of the 2004 Sumatra tsunami in Drake Passage. *Geophysical Research Letters, 38*, L16604.

Saito, M. (1967). Excitation of free oscillations and surface waves by a point source in a vertically heterogeneous Earth. *Journal of Geophysical Research, 72*, 3689–3699.

Simon, J. D., Simons, F. J., & Irving, J. C. E. (2021). A MERMAID miscellany: Seismoacoustic signals beyond the *P* wave. *Seismological Research Letters, 92*, 3657–3667.

Vitousek, M., & Miller, G. (1970). An instrumentation system for measuring tsunamis in the deep ocean. In W. M. Adams (Ed.), *Tsunamis in the Pacific Ocean* (pp. 239–252). East-West Center.

Ward, S. N. (1980). Relationships of tsunami generation and an earthquake source. *Journal of Physics of the Earth, 28*, 441–474.

Wares, G. W., Champion, K. W., Pond, H. L., & Cole, A. E. (1960). Model atmospheres. In *Handbook of geophysics* (pp. (1-1)–(1-43)). The Macmillan Co.

Watada, S., Kusumoto, S., & Satake, K. (2014). Travel-time delay and initial phase reversal of distant tsunamis coupled with the self-gravitating elastic Earth. *Journal of Geophysical Research, Solid Earth, 119*, 4287–4310.

Watanabe, S., Hamilton, K., Sakazaki, T., & Nakano, M. (2022). First detection of the Pekeris internal global atmsopheric resonance: Evidence for the 2022 Tonga eruption and from global reanalysis data. *Journal of Atmospheric Sciences, 79*, 3027–3043.

Wessel, P., & Smith, W. H. F. (1991). Free software helps map and display data. *Eos, Transactions of the American Geophysical Union, 72*, 441 and 445–446.

Wharton, W. J. L. (1888). On the seismic sea waves caused by the eruption of Krakatoa, August 26th and 27th, 1883. In G. J. Symons (Ed.), *The eruption of Krakatoa and subsequent phenomena* (pp. 89–151). Trübner and Co.

Yu, G.-K., & Mitchell, B. J. (1979). Regionalized shear velocity models of the Pacific upper mantle from observed Love and Rayleigh wave dispersion. *Geophysical Journal of the Royal Astronomical Society, 57*, 311–341.